

1 **Patient-specific cell communication networks associate with disease** 2 **progression in cancer**

3
4

5 David L Gibbs¹, Boris Aguilar¹, Vésteinn Thorsson¹, Alexander V Ratushny², Ilya Shmulevich¹

6

7 ¹Institute for Systems Biology, 401 Terry Avenue North, Seattle, WA 98109, USA; ²Bristol-
8 Myers Squibb, 400 Dexter Avenue North, Suite 1200, Seattle, WA 98109, USA

9

10 Correspondence:

11 David L Gibbs

12 david.gibbs@isbscience.org

13

14 **Abstract**

15

16 The maintenance and function of tissues in health and disease depends on cell-cell communication. This
17 work shows how high-level features, representing cell-cell communication, can be defined and used to
18 associate certain signaling 'axes' with clinical outcomes. Using cell-sorted gene expression data, we
19 generated a scaffold of cell-cell interactions and define a probabilistic method for creating per-patient
20 weighted graphs based on gene expression and cell deconvolution results. With this method, we generated
21 over 9,000 graphs for TCGA patient samples, each representing likely channels of intercellular
22 communication in the tumor microenvironment. It was shown that particular edges were strongly
23 associated with disease severity and progression, in terms of survival time and tumor stage. Within
24 individual tumor types, there are predominant cell types and the collection of associated edges were found
25 to be predictive of clinical phenotypes. Additionally, genes associated with differentially weighted edges
26 were enriched in Gene Ontology terms associated with tissue structure and immune response. Code, data,
27 and notebooks are provided to enable the application of this method to any expression dataset
28 (<https://github.com/IlyaLab/Pan-Cancer-Cell-Cell-Comm-Net>).

29 **Keywords**

30 Networks, cell communication, immuno-oncology, computational oncology, bioinformatics, systems
31 biology

32 **Introduction**

33 The maintenance and function of tissues depends on cell-cell communication (Wilson et al., 2000; Haass
34 and Herlyn, 2005). While cell communication can take place through physically binding cell membrane
35 surface proteins, cells also release ligand molecules that diffuse and bind to receptors on other cells

36 (paracrine or endocrine), or even the same cell (autocrine), triggering a signaling cascade that can
37 potentially activate a gene regulatory program (Cameron and Kelvin, 2013; Heldin et al., 2016; Cohen
38 and Nelson, 2018). More generally, a message is sent and received, transferring some information as part
39 of a large network (Frankenstein et al., 2006). Cells communicate in order to coordinate activity, such as,
40 to correctly (and jointly) respond to environmental changes (Song et al., 2019).

41 Altered cellular communication can cause disease, and conversely diseases can alter
42 communication (Wei et al., 2004). Cancer, once thought of as purely a disease of genetics, is now
43 recognized as being enmeshed in complex cellular interactions within the tumor microenvironment
44 (TME) (Trosko and Ruch, 1998). The cell-cell interactions are important for cell differentiation, tumor
45 growth (West and Newton, 2019), and response to therapeutics (Kumar et al., 2018).

46 Between cells, information transfer is directional in nature, where cells produce molecules that
47 are received by the properly paired, and expressed, receptor. There is often a sender and receiver, which
48 makes the cell-cell networks directionally linked by molecules. The dynamics of the signal is greatly
49 important (Fridman et al., 2012, Behar et al., 2013), but unfortunately is difficult to detect in bulk
50 sequencing experiments. One approach to studying cell interactions is through the use of graphical
51 models of communication networks (Morel et al., 2017). By incorporating experimental data, the
52 graphical models can become quantitative, providing predictions that can be tested and used in
53 discovering novel drug targets and developing optimal intervention strategies.

54 In recent work (Thorsson et al., 2018), we developed a method used to identify cellular
55 communication networks at work in the tumor microenvironment. Given a set of samples with a similar
56 tumor microenvironment, the method identified ligands, receptors and cells meeting certain criteria of
57 abundance and concordance within that set of samples. The method was applied to identify networks
58 playing a role within specific tumor types and molecular subtypes and is available as a workflow and
59 interactive module on the iAtlas portal for immuno-oncology (Eddy et al., 2020).

60 In this work, we have combined multiple sources of data with a new probabilistic method for
61 constructing *patient*-specific cell-cell communication networks (Figure 1). In total, we built networks for
62 9,234 samples in The Cancer Genome Atlas (TCGA), starting from a network of 64 cell types and 1,894
63 ligand-receptor pairs. This is a rich feature set from which to investigate biological alterations in cell
64 communication within the tumor microenvironment. We identified informative network features that are
65 associated with disease progression. The method can be applied to any cancer type, but in this manuscript
66 we focus on a selection of cancer types with very high mortality rates, including pancreatic
67 adenocarcinoma (PAAD), melanoma (SKCM), lung (LUSC), and cancers of the gastrointestinal tract
68 (ESCA, STAD, COAD, READ) (Cancer Genome Atlas Network, 2015).

69 This represents a new method that provides information on possible modes of intercellular
70 signaling in the TME, something that is currently lacking. While there are many methods on gene set
71 scoring, cellular abundance estimation, differential expression, there are still few ways to investigate cell-
72 cell communication diversity in the TME with respect to patient outcomes. Fortunately, new databases of
73 receptor-ligand pairs are becoming available, making work in this area possible (Efremova et al., 2019;
74 Jin et al., 2020; Nath and Leier, 2020; Shao et al., 2020). The methods, code, data, and complete results
75 are available and open to all researchers (<https://github.com/IlyaLab/Pan-Cancer-Cell-Cell-Comm-Net>).

76 Methods

77 Data aggregation and integration

78 Data sources including TCGA and cell-sorted gene expression, bulk tumor expression, cell type scores,
79 cell-ligand and cell-receptor presence estimations were used for network construction and probabilistic
80 weighting on a per-sample basis.

81
82 Each tumor sample is composed of a mixture of cell types including tumor, immune, and stromal cells.
83 Recently, methods have been developed to 'deconvolve' mixed samples into estimated fractions of cell
84 type quantities. For example, xCell, which resembles gene set enrichment, has performed this estimation
85 for 64 cell types across most TCGA samples (Aran et al., 2017). We use these xCell estimates of cellular
86 fractions in this work.

87
88 Ramilowski et al. performed a comprehensive survey of cellular communication, generating a
89 compendium that includes 1,894 ligand-receptor pairs, and a mapping between 144 cell types and
90 expression of ligand or receptor molecules (Ramilowski et al., 2015) The compendium was shared via 5th
91 edition of the FANTOM Project, FANTOM5. These ligand-receptor pairs were adopted for this study.
92 Unfortunately, the FANTOM5 collection of cell types does not overlap well with cell types in xCell. In
93 order to integrate the xCell and FANTOM5 data resources, it was necessary to determine the expressed
94 ligands and receptors for each of the 64 cell types in xCell, using the source gene expression data.

95
96 The xCell project used six public cell sorted bulk gene expression data sets in order to generate gene
97 signatures and score each TCGA sample. Across the data sets, there is some discrepancy in cell type
98 nomenclature, making it necessary to manually curate cell type names to improve alignment across
99 experiments (Supplementary Table 1). Typically, for a given cell type, there are several replicate
100 expression profiles, often across the data sets.

101 Building the cell-cell communication network scaffold

102
103 In the FANTOM5 'draft of cellular communication', an expression threshold of 10 TPMs was used to link
104 a cell type to a ligand or receptor. When considering the distribution of expression in the FANTOM5
105 project, 10 TPMs is close to the median.

106
107 To construct our scaffold, we used a majority voting scheme based on comparing expression levels to
108 median levels. For each cell type, paired with ligands and receptors, if the expression level was greater
109 than the median, it was counted as a vote (i.e., ligand expressed in this cell type). If a ligand or receptor
110 received a majority vote across all available data sources, it was accepted, and entered into the cell-cell
111 scaffold.

112
113 With this procedure, a network scaffold is induced, where cells produce ligands that bind to receptors on
114 receiving cells. One edge in the network is composed of components cell - ligand - receptor - cell. This
115 produced a cell-cell communication network with over 1M edges. Each edge represents a possible

116 interaction in the tumor microenvironment. We subsequently determine the probability that an edge is
117 active in a particular patient sample using a probabilistic method described below.

118 Patient level cell-cell communication network weights

119 With a cell-cell scaffold, expression values and cell type estimations per sample, we can produce a per-
120 sample weighted cell-cell communication network (Figure 2). This is done probabilistically, using the
121 following definition:

$$122$$
$$123 P(e_i) = P(l_a, c_l) \cdot P(r_b, c_r), \text{ (Eq. 1)}$$
$$124$$

125 where e_i is edge i , l_a is ligand a , r_b is receptor b , and c_l and c_r are cells that can produce ligand a and
126 receptor b respectively. $P(e_i)$ represents a probability that edge i is active and is based on the premise that
127 the physical and biochemical link and activation is possible only if all the components are present, and
128 that activity becomes increasingly possible with greater availability of those components. The joint
129 probabilities can be decomposed to:

$$130$$
$$131 P(l_a, c_l) = P(l_a | c_l) P(c_l) \text{ and}$$
$$132 P(r_b, c_r) = P(r_b | c_r) P(c_r). \text{ (Eq. 2)}$$
$$133$$

134 The $P(c_{lk})$ is short for CDF $P(C_l < c_{lk})$ which indicates the probability that a randomly sampled value
135 from the empirical C_l distribution (over all 9K TCGA samples) would be less than the cell estimate for
136 cell type l , in sample k . To do this, for a given cell type, using all samples available, an empirical
137 distribution $P(C_l)$ is computed, and for any query, essentially using a value c_{lk} , the probability can be
138 found by integrating from 0 to c_{lk} .

139
140 To compute $P(l_a | c_l)$, each C_l distribution was divided into quartiles, and then (again using the 9K
141 samples) empirical gene expression distributions within each quartile were fit. This expresses the
142 probability that with an observed cell quantity (thus within a quartile), the probability that a randomly
143 selected gene expression value (for gene l_a) would be lower than what is observed in sample k .

144
145 We refer to "edge weights" to be the probability as shown in Eq. (1). To compute edge weights, each
146 TCGA sample was represented as a column vector of gene expression and a column vector of cell
147 quantities (or enrichments). For each edge in the scaffold (cell-ligand-receptor-cell), data was used to look
148 up probabilities using the defined empirical distributions and taking products for the resulting edge
149 weight probability. This leads to over 9K tumor-specific weighted networks, one for each TCGA
150 participant.

151
152 Probability distributions were precomputed using the R language empirical cumulative distribution
153 function (ecdf). For example, fitting $P(\text{CD8 T cells})$ is done by taking all available estimates across the
154 Pan-Cancer samples and computing the ecdf. Then, for a sample k , we find $P(C_l < c_{lk})$ using the ecdf.
155 The same technique is used to find the conditional probability functions, where for each gene, the
156 expression values are selected after binning samples using the R function 'quantile', and then used to
157 compute the ecdf. With all distributions precomputed, 9.8 billion joint probability functions were

158 computed using an HPC environment, then transferred to a Google BigQuery table where analysis
159 proceeded. This table of network weights was structured so that each row contained one weight from one
160 edge and one tumor sample. Although being a large table of 9.8 billion rows, taking nearly 500GB,
161 BigQuery allows for fast analytical queries that can produce statistics using a selection of standard
162 mathematical functions.

163 Association of network features and survival-based phenotypes

164 The S_I statistic is a robust measure based on the difference of medians (Yahaya et al., 2004; Ahad et al.,
165 2016; Babu et al., 1999; Hubert et al. 2012), in this case the median of edge weights for a defined
166 phenotypic group. S_I statistics were computed using the NCI cancer research data commons cloud
167 resource, the ISB-CGC, per tissue type.

168

$$169 \quad S_I = \frac{\text{median}(X) - \text{median}(Y)}{\sqrt{1.4826 \text{MAD}(X) + 1.4826 \text{MAD}(Y)}}$$

170

171 This statistic allowed for cell-cell interactions to be ranked within a defined context. The results were
172 again saved to BigQuery tables to allow for further cloud-based analysis and integration with underlying
173 data.

174

175 To judge the magnitude of the statistic with respect to a random context (Figure 3), an ensemble of three
176 edge-weight sample-pools were generated, each with 100K weights. Then, for each member of the
177 ensemble, 1 million S_I statistics were generated using sample sizes that match the analyzed data. These
178 random S_I statistic distributions were used to compare to the observed results (i.e., a resampling
179 procedure).

180

181 As an initial examination of the interplay of cell communication and disease, two proxies of disease
182 severity were investigated: progression-free interval (PFI) and tumor stage (Liu et al., 2018). The staging
183 variable used the AJCC pathologic tumor stage. The PFI feature was computed using days until a
184 progression event. The staging variable was binarized by binning stages I-II together (“early stage”), and
185 III-IV together (“late stage”). A binary PFI variable was created by computing the median PFI on non-
186 censored samples and then applying the split to all samples. Both clinical features were computed by
187 tissue type (TCGA Study). As Liu et al writes, "The event time is the shortest period from the date of
188 initial diagnosis to the date of an event. The censored time is from the date of initial diagnosis to the date
189 of last contact or the date of death without disease."

190

191 For example, in LUSC, the median time to PFI event was 420 days (14.0 months) and in the censored
192 group, 649 days (21.1 months). After splitting samples at 420 days (14 months), the short PFI group was
193 composed of 67 uncensored samples and 128 censored samples. The long PFI group was composed of 68
194 uncensored samples and 234 censored samples.

195

196 Null distributions, using these same sample sizes (e.g., one group of 68 and another group of 234), were
197 generated by repeatedly drawing from the previously described ensemble of three sample-pools. The
198 distributions, while heavy tailed, were close to Normal (Supplemental Figure 1). The S_I statistics scale

199 with the difference in median values (Supplemental Figure 4). After combining resampled statistics across
200 the ensemble, an edge was selected as a high edge weight if it were in the top 1 millionth percentile when
201 compared to the null. Each tissue and contrast generates a weighted subgraph of the starting scaffold,
202 which is retained for further analysis (e.g., a LUSC-PFI network).

203
204 To identify informative cell-cell edges that relate to disease progression, machine learning models were
205 trained on binarized clinical data as described. With clinical features such as progression free interval
206 (PFI) and tumor stage for each sample, a matrix of patient-specific edge weights was constructed
207 representing each tissue and contrast. Classification of samples was performed with XGBoost classifiers
208 (Chen and Guestrin, 2016), which are composed of an ensemble of tree classifiers. To avoid overfitting
209 the models, the tree depth was set at maximum of 2 and the early-stopping parameter was set at 2 rounds
210 (training was stopped after the classification error did not improve on a test set for two rounds). XGBoost
211 provides methods for determining the information gain of each feature in the model and was used to rank
212 edges that are most informative for classification.

213
214 Gene ontology (GO) term enrichment was performed using the GONet tool (Pomaznoy et al., 2018). The
215 set of 1,175 genes in the cell-cell scaffold was used as the enrichment background. GONet builds on the
216 "goenrich" software package, which maps genes onto terms and propagates them up the GO graph,
217 performs Fisher's exact tests, and moderates results with FDR. To compare the results, random collections
218 of genes were generated from the cell-cell scaffold and produced no significant results.

219 Results

220 The scaffold network graph is heterogeneous, containing nodes representing cells, ligands (e.g.
221 cytokines), and receptors. Edges are directed, following communication routes from cell to cell. But, to
222 simplify the graph, a cell produces a ligand that binds a receptor found on another cell type, which could
223 make a single edge "LCell-Ligand-Receptor-RCell". In total, there were 1,062,718 cell-cell edges in the
224 network.

225
226 The number of edges for ligand-producing cells varies from 32,910 for osteoblasts to 6,587 for Multi-
227 Potent Progenitor (MPPs). For receptor-producing cells, the range spans from 30,225 for platelets to
228 5,763 edges for MPPs.

229
230 Applying the proposed probabilistic framework allowed for the creation of 9,234 weighted networks. The
231 edge weight distributions generally follow approximately exponentially decreasing function
232 (Supplemental Figure 1). There are few edges with strong weights and many with low (near zero)
233 weights.

234
235 We first sought to find communication edges that were most characteristic of an individual tumor type.
236 The S_I statistics comparing one tumor type to all other tissue types was computed, with a high score
237 indicating a substantial difference in edge weights between the two groups. Edges were found that clearly
238 delineated tissues (Figure 4). For example, in SKCM (skin cutaneous melanoma), the top scoring edge is
239 between melanocytes the most cell of origin for cutaneous melanoma (Melanocytes-MIA-CDH19-
240 Melanocytes, S_I score 2.5, median edge weight 0.86 higher than in other tumor types). Normal tissue

241 differences can contribute to differences in edge weights, though in this case the central role of
242 melanocytes in melanomas implies that the high scores are likely due to cancerous cell activity. The study
243 with the most similar edge weights is uveal melanoma (UVA), which arises from melanocytes resident in
244 the uveal tract (Robertson et al., 2017) (Fig. 4A). Additionally, we observed that when a cell type is
245 highly prevalent in a particular tissue, and the scaffold has an autocrine loop, interactions between that
246 type of cell tend to have high weights. If we exclude cell types communicating with self-types, then for
247 SKCM, osteoblasts, natural killer T cells, and mesenchymal stem cells (MSCs) interact with melanocytes
248 in the top 10 scoring edges, consistent with the emerging role of these cell types in melanoma. An
249 important role for osteoblasts is now coming to light for melanoma (Ferguson et al., 2020). Natural killer
250 T cells are being investigated for their applicability in immunotherapy of cancers such as melanoma
251 (Wolf et al., 2018). MSCs appear to interact with melanoma cells, as work by Zhang et al. (Zhang et al.,
252 2017) showed the proliferation of A375 cells (a melanoma cell line) was inhibited and the cell cycle of
253 A375 was arrested by MSCs, and cell-cell signaling related to NF- κ B was down-regulated. Overall, the
254 number of high weight edges in each tumor type did not associate with the number of samples, as might
255 be expected (Supplemental Figure 2).

256
257 To identify which elements of cellular communication networks might be associated with clinical
258 progression of particular tumor types, we identified edges associated with disease.
259 Disease progression and severity were examined using dichotomous values of tumor stage and
260 progression free interval (PFI) as described in the methods. Statistical scores were calculated comparing
261 edge weight distributions between the two clinical groups using S_I . Results were carried forward if larger
262 than the threshold set by the millionth percentage of resampled statistics (Supplemental Figure 3-5),
263 yielding differentially weighted edges (DWEs).

264
265 Most tumor types showed DWEs for PFI, and fewer for the early to late tumor stage comparison
266 (Supplemental Figure 5). For example, STAD (gastric adenocarcinoma) had several hundred edges in for
267 both comparisons, while PAAD (pancreatic adenocarcinoma) showed fewer DWEs, and only for PFI.
268 Figure 5 shows median edge weights between the two groups for the selected studies. Some tumor types,
269 like SKCM, show much stronger deviations between the medians, compared to the other studies like
270 STAD, ESCA, and LUSC, which may be an indication of a stronger immune response. According to
271 CRI-iAtlas (Eddy et al., 2020), among our example studies, SKCM has the highest estimated level of
272 CD8 T cells and generally has a robust immune response.

273 Tumor stage comparison showed DWEs in 17 of 32 studies and ranged widely from 4 edges for
274 MESO (mesothelioma) to over 63K edges for BLCA (urothelial bladder cancer adenocarcinoma). The
275 PFI comparison showed results in 28 / 32 studies and ranged from 4 edges in READ to over 21K in
276 LIHC. See Table 1 for edge counts from selected studies. The studies with larger numbers of samples had
277 permuted S_I distributions that were narrow compared to studies with few samples (Supp. Fig. 3), but there
278 was not a strong association between DWE counts and sample sizes. The variation thus more likely has to
279 do with clinical factors.

280
281 Within a tumor type and clinical response variable, the set of high scoring edges were usually dominated
282 by a small number of cell-types, ligands, or receptors (Figure 6, Supplemental Figure 6A,6B). For SKCM,
283 in the tumor stage contrast, a majority of ligand-producing cells include GMP cells, Osteoblasts, MSC
284 cells, and Melanocytes, in order of prevalence. The number of edges starting with these four cells

285 accounts for 53% of DWEs. Certainly, melanocytes are well known in melanoma, and mesenchymal stem
286 cells are drawn to inflammation, but the role of osteoblasts is less well documented, but still have been
287 associated with melanoma progression (Ferguson et al., 2020).

288 In the PFI contrast with gastroesophageal cancers, megakaryocytes are the most common cell
289 type in STAD DWEs (40 edges out of 142), and the second most common in ESCA (49 edges out of 137,
290 following CD8+ Tcm interactions). The megakaryocyte DWEs include ligands and receptors that
291 represent both interleukins and ECM-associated molecules such as integrins and collagen, but also
292 NOTCH1 and PF4 (platelet factor 4). For STAD, most edge weights are lower with longer PFI. Put
293 another way, the shorter PFI intervals (adverse outcome) were associated with increased megakaryocyte-
294 involved edge weights (Supplemental Figure 7).

295 However, the opposite is observed in ESCA, where higher edge weights were generally
296 associated with longer PFI (negative S_I score). In ESCA, edges that show high weights for short PFI
297 include Neutrophils-HMGB1-SDC1-Sebocytes (0.17). Although ESCA has a much lower xCell mean
298 megakaryocyte score than STAD (38% lower), the cell score trends from xCell follow opposite trends
299 with STAD decreasing with longer PFI and ESCA increasing with PFI. STAD is among the tissues with
300 highest megakaryocyte scores (59, 56th rank out of 64 for PFI 1,2 resp.), ESCA is at a respectable rank of
301 49 and 44 out of 64 for short-PFI, respectively.

302 In COAD (colorectal adenocarcinoma), for ligand-producing cells, the DWEs were dominated by
303 astrocytes, MSCs, megakaryocytes, and sebocytes, while receptor-producing cells included astrocytes,
304 chondrocytes, and MSCs in order of counts of DWEs. By summarizing DWEs we can possibly categorize
305 cancer types based on which cells are taking part in potentially active interactions.

306 The above-described edge dominance is related to cells (graph nodes) with high degree. In the
307 language of graphs, the degree is the count of edges connected to a given node or vertex. In STAD the
308 cell types with highest degree are megakaryocytes (degree 50), followed by neutrophils (31), CLP cells
309 (26), and erythrocytes (23)(Supplemental Figure 6A,B). However, if we look at the directionality for the
310 directed graph, we see that while megakaryocytes are split nearly evenly in and out, cells like the Th1
311 have 5 edges in, and only a single edge out, whereas B cells have zero edges in and 4 edges out. The
312 network directionality should be considered in activities such as the modeling of dynamical systems.

313
314 Within the tumor microenvironment, communication between the multitude of cells happens
315 simultaneously through many ligand-receptor axes. By considering a set of differentially weighted edges
316 within a tissue type, we can construct connected networks that potentially represent dynamic
317 communication. DWEs derived by comparing edge weights between clinical groups may indicate which
318 parts of the cell-cell communication network shift together with disease severity.

319 We sought to identify which aspects of intercellular communication could relate to tumor staging
320 or disease severity. The edges making up the differential networks were used to model clinical states for
321 individual tumors. XGBoost models (Chen and Guestrin, 2016) were fit on each clinical feature, using
322 edge weights as predictive variables, to infer which edges carried the most information in classification
323 (Figure 8).

324 The purpose of the modeling was within-data inference rather than classification outside of the
325 TCGA pan-cancer data set. After fitting, it is possible to examine what model features (edges) are most
326 useful in classification. The XGBoost classifiers are regularized models, not all features will be used and
327 often only a small subset of features are retained in the final model. We assess the relative usefulness of a
328 feature by comparing the feature gain -- the improvement in accuracy when a feature is added to a tree.

329 All classification models had an accuracy between 91% (SKCM, PFI) and 99% (COAD, Stage). As
330 mentioned above, there can be a high degree of correlation between edge values in a data set. While
331 features are selected first based on improving prediction, the machine learning model accounts for
332 correlated features by selecting the one that has best predictive power, leaving out other correlated
333 features. That said, the number of features selected by the model is then related to the correlation
334 structure. In a set of uncorrelated features where all features add to the predictive power, all features will
335 be selected, whereas for correlated features, only a small number will be selected. This is seen in results
336 here in terms of differences in the numbers of features compared with the starting network.

337 In the COAD-PFI case, the number of features was reduced by approximately 20%, keeping 50
338 edges in the model. The STAD-PFI features were reduced by approximately 45%. Other examples are are
339 LUSC-PFI at 60% reduction, ESCA-PFI at 74%, and SKCM-PFI at 95% (12 edges selected) indicating a
340 high degree of internal feature correlation.

341 A similar pattern was observed in the tumor stage contrasts, where SKCM-stage had a 96%
342 reduction in features, STAD-stage 52%, READ-stage 47%. For COAD-stage, feature reduction was 95%
343 reduction, but attributable to the large number of starting edges (1851) compared to the 84 edges selected.
344 A collection of the most predictive edges is given in Table 2.

345
346 The collection of genes from each differential network was used for gene ontology (GO) term enrichment
347 using the GONet tool (Pomaznoy et al., 2018). All tissue-contrast combinations with differentially
348 weighted edges produced enriched GO terms (FDR < 0.05, within tissue contrasts) except the SKCM-
349 stage group, which although contained 77 genes in the differential network, produced no enriched terms.

350 Common themes included structural GO terms such as "extracellular structure organization" (for
351 SKCM), cell-substrate adhesion (ESCA, LUSC), cell-cell adhesion (STAD), ECM / extracellular matrix
352 organization (LUSC, COAD, READ, STAD). Cell migration was also a common theme with "cell
353 migration" (STAD), "epithelial cell migration" (SKCM), and "regulation of cell migration" (LUSC,
354 COAD/READ). Among immune related themes, GO terms included "IFNG signaling" and "antigen
355 processing and presentation" (SKCM), "regulation of immune processes" and "IL2" (STAD), and "viral
356 host response" (COAD / READ). See Table 3 for a summary and supplemental table 3 for complete
357 results.

358 Discussion

359 Patient outcome or response to therapy is not necessarily well predicted by tumor stage alone (Kirilovsky
360 et al., 2016). As Fridman et al. wrote, "different types of infiltrating immune cells have different effects
361 on tumour progression, which can vary according to cancer type" (Fridman et al., 2012). This idea has
362 been developed further with the creation of the 'Immunoscore', a prognostic based on the presence and
363 density of particular immune cells in the TME context, expanded to include the peripheral margin as well
364 as tumor core. For example, the Immunoscore in colorectal cancer depends on the density of both CD3+
365 lymphocytes (any T cell) and specifically, CD8+ cytotoxic T cells in the tumor core and invasive margin
366 (Pagès et al., 2018). The differences in factors that relate to stage and survival is reflected in the current
367 work in the identification of different cell-cell interactions of importance for each.

368
369 Previous studies have shown that cellular interactions within the tumor microenvironment have an
370 impact on patient survival, drug response, and tumor growth. X. Zhao et al. (Zhou et al., 2017) described

371 alterations in ligand-receptor pair associations in cancer compared to normal tissue, the cell-cell
372 communication structures thereby becoming a generalized phenotype for malignancy. Using the same
373 foundational database of possible interactions as this work, ligand-receptor pair expression correlation
374 was compared between tumor and normal tissue. Their "aggregate analysis revealed that ... tumors of
375 most cancer types generally had reduced (ligand-receptor) correlation compared with the normal tissues."
376 The ligand-receptor pairs that commonly showed such differences across the ten tissue types studied
377 included PLAU-ITGA5, LIPH-LPAR2, SEM14G-PLXNB2, SEMABD-TYROBP, CCL2-CCR5, CCL3-
378 CCR5, and CGN-TYROBP.

379
380 Like the Zhao et al. work, we found the collection of associated edges enriched for related biological
381 processes, especially to ECM organization and cell adhesion -- possibly related to the progression towards
382 dysplasia. For example, in Zhao et al., the ligand-receptor pairs COL11A1-ITGA2, COL7A1-ITGA2,
383 MDK-GPC2 and MMP1-ITGA2 were found to be positively correlated in cancer but not in normal tissue.
384 In the current work, integrins and laminins generally have elevated edge weights in late tumor stage. In
385 the PFI contrasts, except for ESCA, such edges have higher weights in shorter PFIs, corresponding to
386 more severe progression. Regarding SEMA7A, found in the PFI STAD results as a predictive feature,
387 previous findings report the collagen gene COL1A1 has been associated with metastasis, and SEMA7A is
388 known to play an important role in integrin-mediated signaling and functions both in regulating cell
389 migration and immune responses. Cancers such as esophageal, gastric, and colorectal all show transitions
390 to metaplasia and dysplasia, a process that breaks down the structural order of a tissue, replacing it with
391 disorder and cell transdifferentiation.

392
393 In our model, a host response is reflected in a change in S_I score, negative if the edge weight is higher
394 with longer PFI times. In the PFI results, Th1 cells appeared in 13 high scoring edges in SKCM, all with
395 negative S_I values. Also, for SKCM and COAD, ligand producing (pro-inflammatory) M1 macrophage
396 edges are present but show both positive and negative S_I scores. Inflammation cytokines IL1B and IL18
397 are both present in the results of ESCA and STAD (Figure 9). In the tumor stage contrasts, we see Th2
398 and NK cells with inflammation cytokines IL1A, IL1B, IL4, TNF in STAD and COAD. So, while certain
399 inflammatory signatures are observed, the absence of well-known canonical edges such as Th1-IL12-
400 IL12RB1-M1 macrophages, may be due to essentially no difference, or undetectable differences in the
401 quantity of Th1 cells or IL12A expression between PFI groups (4.9 vs 3.3 TCGA Pan-Cancer RSEM for
402 short vs long PFI). These observations point to possible mechanisms of action for immune cells known to
403 be important for cancer immune response, the CD4+ T helper 1 cells and M1 macrophages, in relation to
404 tumor progression

405
406 In tissues susceptible to dysplasia, such as the tissues explored here, unexpected cell types may be
407 detected. For example, the "...disruption of tissue organization appears to trigger a profound change in
408 cellular commitment, which leads to hepatocyte differentiation in the "oval cells" in ... the epithelial
409 cells lining the small pancreatic ductules' (Reddy et al., 1991). As another example, pancreatic cancer is
410 known to have desmoplastic stroma, the source of which may include MSCs which are defined by their
411 ability to differentiate into osteoblasts, chondrocytes, and adipocytes (Mathew et al., 2016). In line with
412 that finding, it's been observed that "...stromal cells isolated from the neoplastic pancreas can differentiate
413 into osteoblasts, chondrocytes, and adipocytes" (Mathew et al., 2016).

414

415 It has been reported that (Yáñez et al., 2017), "granulocyte-monocyte progenitors (GMPs) and monocyte-
416 dendritic cell progenitors (MDPs) produce monocytes during homeostasis and in response to increased
417 demand during infection." or as in (Weston et al., 2018), "Granulocyte-monocyte progenitor (GMP) cells
418 play a vital role in the immune system by maturing into a variety of white blood cells, including
419 neutrophils and macrophages, depending on exposure to cytokines such as various types of colony
420 stimulating factors (CSF)."

421
422 In our results for SKCM and COAD, GMPs had negative S_1 statistics, meaning the late-stage cases had
423 edges with higher weights. The GMP cells most often interacted with (as receptor bearing cells) MSC,
424 Melanocytes, both M1 and M2 macrophages, and CD8+ Tem (T effector-memory cells). The presence of
425 GMP related edges may be indicative of the commonly observed 'myeloid dysfunction', which "can
426 promote tumor progression through immune suppression, tissue remodeling, angiogenesis or
427 combinations of these mechanisms."(Messmer et al., 2015) Also, "tumors secrete a variety of factors such
428 as G-CSF that act in a systemic way to reduce IRF-8 within progenitor cells, releasing myelopoiesis from
429 IRF-8 control such that the granulocytic lineage (blue cell) undergoes hyperplasia, leading to increased
430 immature suppressive cells to promote tumor growth." This is in line with our observations.

431
432 Megakaryocytes, a multipotent stem cell, are cells that typically reside in the bone marrow and produce
433 platelets. Megakaryocytes are also produced in the liver, kidney, and spleen. Additionally,
434 megakaryocytes have been observed in the lung and circulating blood where they were useful as a
435 biomarker in prostate cancer. Case reports exist showing megakaryocytes in the metaplasia of gastric
436 cancer patients (Chatelain et al., 2004). Megakaryocytes respond to a variety of cytokines such as IL-3,
437 IL-6, IL-11, CXCL5, CXCL7, and CCL5. A majority of interacting cells are leukocytes. In both
438 esophageal and gastric cancers "...thrombocytosis has been reported in general to be associated with
439 adverse clinical outcomes. (Voutsadakis, 2014)" Additionally, there are reports of 'tumor educated
440 platelets' that can be useful as part of a liquid biopsy (Best et al., 2018) (Haemmerle et al., 2018).

441
442 Among the rich literature regarding oncological cytokine networks, there is a strong emphasis on the
443 cancer cell as a central actor. Many of the review articles and research focuses on the cancer cell
444 interactions in the TME. For example, cancer cells producing an overabundance of IL6 or IL10 that has
445 been associated with poor prognosis (Burkholder et al., 2014; Fisher et al., 2014; Lippitz and Harris,
446 2016).

447
448 However, in this work, the focus has been put on the environment and less about the cancer cell itself.
449 This is largely because in performing cell deconvolution on gene expression data to determine the
450 presence and quantity of different cell types in the mixed sample, reliable signatures for cancer cells are
451 not readily available. Because in carcinomas, a cancer cell derives from the epithelium, and in many
452 ways remains similar to epithelial cells. Even in single cell RNA-seq studies, it is often difficult to
453 determine what cells are cancerous and picking this signature out of a mixed expression dataset is difficult
454 and remains an open question.

455
456 This work is based upon gene expression, rather than protein expression, cell-surface expression or
457 secretion measurements. Also, the base expression data is taken from sorted cells, rather than cells in
458 tissue with an assumption that we cannot get "new/non-scaffold edges" in a tissue/cancer context.

459 However new data types and methods including scRNA-seq and PIC-seq will provide ways of
460 determining new cell-cell interactions that are context specific (Giladi et al., 2020).

461
462 Importantly, the physical and biochemical process of secretion, binding and activation cannot be
463 identified with the current data and method. By identifying the propensity of edge constituents in
464 particular tumor microenvironments in comparison with others, it becomes more likely that
465 communication with activation can take place, as the presence of those constituents is a prerequisite.

466
467 With the data and results publicly available in a Google BigQuery table (Supplemental Figure 8), this
468 resource is open to researchers to explore and ask questions. It is a low-cost way (with free options) to
469 achieve compute cluster performance for quickly answering such questions. The table is easily joined to
470 clinical and molecular annotations and can be worked with from R and python notebooks. With the
471 addition of resources like GTEX, it should begin to be possible to tease aberrant, cancer specific
472 interactions apart.

473
474 In terms of future work, it could be important to examine communication networks given the immune
475 subtypes of (Thorsson et al., 2018) and communication differences between TCGA tumor molecular
476 subtypes. New data types can be applied to enhance the scaffold with knowledge gained from (for
477 example) single-cell RNA-seq.

478
479 In this work, we have introduced a method and identified lines of communication between cells that may
480 play a role in disease. These lines include both established/recognized cells in the context of cancer, as
481 well as others that should be explored further, with targeted methods.

482 Acknowledgments

483 The authors would like to thank Samuel Danziger, David Reiss, Mark McConnell, Andrew Dervan,
484 Matthew Trotter, Douglas Bassett, Robert Hershberg, the Shmulevich Lab and the Institute for Systems
485 Biology for engaging and informative discussions. This study was supported by Celgene, a wholly owned
486 subsidiary of Bristol-Myers Squibb, in part through a Sponsored Research Award to D.L.G., B.A. and I.S,
487 and by the Cancer Research Institute (D.L.G, V.T, I.S). We thank the ISB-CGC for their ongoing support.
488 ISB-CGC has been funded in whole or in part with Federal funds from the National Cancer Institute,
489 National Institutes of Health, Task Order No. 17X148 under Contract No. 75N91019D00024. The content
490 of this publication does not necessarily reflect the views or policies of the Department of Health and
491 Human Services, nor does mention of trade names, commercial products, or organizations imply
492 endorsement by the U.S. Government.

493 Competing Interests.

494 D.L.G., B.A., V.T. and I.S. declare no competing interests. A.V.R.: Bristol-Myers Squibb: Employment,
495 Equity Ownership.

496 **Author Contributions**

497 D.L.G., B.A., V.T, A.R., I.S. conceived of the idea. D.L.G. developed the method, wrote the code, and
 498 performed the computations. D.L.G. wrote the manuscript with contributions from B.A., V.T., A.R., I.S.
 499 and A.R. supervised the project. All authors provided critical feedback and helped shape the research,
 500 analysis and manuscript.
 501

502 **Tables**

503 Table 1. Counts of differentially weighted edges compared to the number of samples in each study.
 504

Study	N samples	PFI short/long	PFI DWEs	Selected Feat.	Model Accuracy	GO results?
ESCA	170	73/97	137	36	94.7	y
STAD	409	155/231	142	78	95.1	y
PAAD	178	68/83	8	-	-	y
COAD	281	96/183	63	50	97.1	y
READ	91	16/71	4	-	-	y
SKCM	102	27/75	249	12	91.1	y
LUSC	494	193/285	304	119	98.7	y
Study	N samples	Stage early/late	Stage DWEs	Selected Feat.	Model Accuracy	GO results?
ESCA	170	86/63	0	-	-	-
STAD	409	167/198	241	114	99.7	y
PAAD	178	142/7	0	-	-	-
COAD	281	151/118	1851	84	99.6	y
READ	91	36/44	34	18	97.5	y
SKCM	102	68/29	221	8	99	n
LUSC	494	390/89	0	-	-	-

505 Study: tissue type, N samples: number of samples used, PFI short/long: number of samples in each group,
 506 PFI DWEs: number of differentially weighted edges, Model Accuracy: accuracy of predicting group, GO
 507 results?: if yes, significant GO enrichments.
 508
 509
 510
 511

512 Table 2. Top 5 most predictive edges from XGBoost models.
513

Contrast	Study	EdgeID	LCell	Ligand	Receptor	RCell	S1	Median Diff	Information Gain
PFI	COAD	586640	Megakaryocytes	BMP10	ENG	Epithelial cells	0.169	0.082	0.109
PFI	COAD	50871	astrocytes	TNC	ITGA5	mv Endothelial cells	0.168	0.061	0.069
PFI	COAD	406871	Hepatocytes	GDF2	ENG	Epithelial cells	0.168	0.082	0.067
PFI	COAD	49669	astrocytes	EFNB1	EPHB4	Mesangial cells	0.199	0.117	0.066
PFI	COAD	632560	MEP	TIMP2	ITGB1	MEP	0.167	0.095	0.051
Stage	COAD	406579	Hepatocytes	CGN	TGFBR2	Eosinophils	-0.165	-0.077	0.043
Stage	COAD	330377	Eosinophils	LAMB3	ITGB1	Eosinophils	-0.144	-0.048	0.038
Stage	COAD	616033	Memory B-cells	BMP15	BMP2	Epithelial cells	-0.150	-0.060	0.037
Stage	COAD	784400	NK cells	TNFSF10	TNFRSF10B	CD4+ memory T-cells	0.137	0.043	0.037
Stage	COAD	630108	MEP	B2M	KIR2DL1	iDC	0.138	0.055	0.037
PFI	ESCA	457801	Keratinocytes	GS	ADCY7	CD4+ Tcm	0.167	0.078	0.078
PFI	ESCA	182483	CD8+ Tcm	RBP3	NOTCH1	pDC	-0.184	-0.073	0.071
PFI	ESCA	1051114	Th2 cells	CALM1	GP6	naive B-cells	0.171	0.085	0.070
PFI	ESCA	658080	Mesangial cells	SPP1	CD44	Tregs	0.184	0.080	0.064
PFI	ESCA	397215	GMP	HMGB1	THBD	MEP	0.184	0.060	0.059
PFI	LUSC	879775	Plasma cells	VEGFA	ITGB1	GMP	0.120	0.047	0.041
PFI	LUSC	451902	iDC	VEGFA	ITGB1	Plasma cells	0.137	0.067	0.038
PFI	LUSC	398971	GMP	ADAM17	ITGB1	Plasma cells	0.120	0.059	0.030
PFI	LUSC	340857	Epithelial cells	COL4A6	ITGB1	CD8+ naive T-cells	0.124	0.054	0.026
PFI	LUSC	471558	Keratinocytes	THBS1	ITGA6	Plasma cells	0.120	0.068	0.025
Stage	READ	632552	MEP	TGFB3	TGFBR2	MEP	-0.267	-0.134	0.127
Stage	READ	795527	NKT	GZMB	PGRMC1	CD4+ memory T-cells	0.343	0.144	0.115
Stage	READ	402754	Hepatocytes	CGN	TGFBR2	CD4+ Tem	-0.274	-0.134	0.108
Stage	READ	808308	NKT	GZMB	IGF2R	Plasma cells	0.261	0.101	0.103
Stage	READ	800747	NKT	IL7	IL2RG	GMP	0.264	0.136	0.095
PFI	SKCM	1008243	Smooth muscle	SEMA7A	PLXNC1	pro B-cells	0.438	0.259	0.242

PFI	SKCM	517677	Macrophages	UBA52	NOTCH1	Osteoblast	-0.284	-0.145	0.200
PFI	SKCM	80934	Basophils	VIM	CD44	NKT	-0.383	-0.254	0.103
PFI	SKCM	1007915	Smooth muscle	PSAP	SORT1	Preadipocytes	0.311	0.175	0.082
PFI	SKCM	84049	Basophils	CALM1	PTPRA	Th1 cells	-0.285	-0.151	0.080
Stage	SKCM	275306	CLP	GI2	CXCR1	Osteoblast	0.353	0.176	0.207
Stage	SKCM	399084	GMP	TIMP1	CD63	Plasma cells	-0.302	-0.147	0.206
Stage	SKCM	273727	CLP	GI2	F2R	MEP	0.290	0.123	0.182
Stage	SKCM	182981	CD8+ Tcm	GI2	TBXA2R	Plasma cells	-0.283	-0.095	0.123
Stage	SKCM	397545	GMP	BST1	CAV1	MSC	-0.337	-0.194	0.109
PFI	STAD	461765	Keratinocytes	CALM3	KCNQ1	Eosinophils	-0.136	-0.067	0.062
PFI	STAD	644724	Mesangial cells	TGFB2	ACVR1	Erythrocytes	0.149	0.061	0.054
PFI	STAD	105991	CD4+ T-cells	IL1B	IL1R2	Megakaryocytes	0.134	0.081	0.047
PFI	STAD	269013	CLP	ADAM28	ITGA4	CD4+ T-cells	0.145	0.075	0.046
PFI	STAD	343620	Epithelial cells	VCAN	TLR1	CLP	0.134	0.051	0.033
Stage	STAD	128412	CD4+ Tem	CALM1	KCNQ1	Macrophages	0.140	0.058	0.057
Stage	STAD	43832	astrocytes	FBN1	ITGB6	Epithelial cells	-0.146	-0.058	0.036
Stage	STAD	346120	Epithelial cells	LAMB1	ITGAV	Hepatocytes	-0.139	-0.066	0.035
Stage	STAD	403540	Hepatocytes	SHH	PTCH1	CD8+ T-cells	-0.138	-0.069	0.034
Stage	STAD	648983	Mesangial cells	FGB	ITGAV	Megakaryocytes	-0.140	-0.060	0.031

514 Contrast: the groupwise test performed, Study: tissue type, Edge ID: BigQuery table lookup ID, LCell:
 515 cell producing ligands, Ligand: ligand gene symbol, Receptor: receptor gene symbol, R Cell: receptor
 516 producing cell, S_1 : between group S_1 statistic, Median Diff: difference in edge weights between groups,
 517 Information Gain: Xgboost information gain after adding feature to model.

518

519 Table 3. Enriched GO terms.

<u>Tissue</u>	<u>Contrast</u>	<u>Num GOs</u>	<u>ECM</u>	<u>Migration</u>	<u>Immune</u>	<u>Immune2</u>
SKCM	PFI	34	extracellular structure organization	epithelium cell migration	IFNG signaling	antigen processing and presentation
ESCA	PFI	3	cell-substrate adhesion			

STAD	PFI	59	cell-cell adhesion mediated by integrin	cell migration	regulation of immune system process	IL2
LUSC	PFI	39	extracellular matrix organization	positive regulation of cell migration		
COAD / READ	stage	85	ECM	regulation of epithelial cell migration	viral host response	
STAD	stage	28	ECM / adhesion	cell migration		

520 Tissue: TCGA study, Contrast: the groupwise test performed, Num GOs: number of gene ontology terms
 521 found significantly enriched, ECM: GO categories involving ECM, Migration: GO terms involving cell
 522 migration, Immune: GO terms involving immune response, Immune2: additional GO terms involving
 523 immune response.

524

525 References

526

527 Ahad, N. A., Yahaya, S. S. S., and Yin, L. P. (2016). Robustness of S1 statistic with Hodges-Lehmann for
 528 skewed distributions. *AIP Conf. Proc.* 1782, 050002.

529 Aran, D., Hu, Z., and Butte, A. J. (2017). xCell: digitally portraying the tissue cellular heterogeneity
 530 landscape. *Genome Biol.* 18, 220.

531 Babu, G. J., Padmanabhan, A. R., and Puri, M. L. (1999). Robust one-way ANOVA under possibly non-
 532 regular conditions. *Biometrical Journal: Journal of Mathematical Methods in Biosciences* 41, 321–
 533 339.

534 Behar, M., Barken, D., Werner, S. L., and Hoffmann, A. (2013). The dynamics of signaling as a
 535 pharmacological target. *Cell* 155, 448–461.

536 Best, M. G., Wesseling, P., and Wurdinger, T. (2018). Tumor-Educated Platelets as a Noninvasive
 537 Biomarker Source for Cancer Detection and Progression Monitoring. *Cancer Res.* 78, 3407–3412.

538 Burkholder, B., Huang, R.-Y., Burgess, R., Luo, S., Jones, V. S., Zhang, W., et al. (2014). Tumor-induced
 539 perturbations of cytokines and immune cell networks. *Biochim. Biophys. Acta* 1845, 182–201.

540 Cameron, M. J., and Kelvin, D. J. (2013). *Cytokines, Chemokines and Their Receptors*. Landes
 541 Bioscience.

- 542 Cancer Genome Atlas Network (2015). Genomic Classification of Cutaneous Melanoma. *Cell* 161, 1681–
543 1696.
- 544 Chatelain, D., Devendeville, A., Rudelli, A., Bruniau, A., Geslin, G., and Sevestre, H. (2004). Gastric
545 myeloid metaplasia: a case report and review of the literature. *Arch. Pathol. Lab. Med.* 128, 568–
546 570.
- 547 Chen, T., and Guestrin, C. (2016). XGBoost: A Scalable Tree Boosting System. in *Proceedings of the*
548 *22Nd ACM SIGKDD International Conference on Knowledge Discovery and Data Mining KDD*
549 '16. (New York, NY, USA: ACM), 785–794.
- 550 Cohen, D. J., and Nelson, W. J. (2018). Secret handshakes: cell-cell interactions and cellular mimics.
551 *Curr. Opin. Cell Biol.* 50, 14–19.
- 552 Eddy, J. A., Thorsson, V., Lamb, A. E., Gibbs, D. L., Heimann, C., Yu, J. X., et al. (2020). CRI iAtlas: an
553 interactive portal for immuno-oncology research. *F1000Res.* 9, 1028.
- 554 Efremova, M., Vento-Tormo, M., Teichmann, S. A., and Vento-Tormo, R. (2019). CellPhoneDB v2.0:
555 Inferring cell-cell communication from combined expression of multi-subunit receptor-ligand
556 complexes. *bioRxiv*. doi:10.1101/680926.
- 557 Ferguson, J., Wilcock, D. J., McEntegart, S., Badrock, A. P., Levesque, M., Dummer, R., et al. (2020).
558 Osteoblasts contribute to a protective niche that supports melanoma cell proliferation and survival.
559 *Pigment Cell Melanoma Res.* 33, 74–85.
- 560 Fisher, D. T., Appenheimer, M. M., and Evans, S. S. (2014). The two faces of IL-6 in the tumor
561 microenvironment. *Semin. Immunol.* 26, 38–47.
- 562 Frankenstein, Z., Alon, U., and Cohen, I. R. (2006). The immune-body cytokine network defines a social
563 architecture of cell interactions. *Biol. Direct* 1, 32.
- 564 Fridman, W. H., Pagès, F., Sautès-Fridman, C., and Galon, J. (2012). The immune contexture in human
565 tumours: impact on clinical outcome. *Nat. Rev. Cancer* 12, 298–306.
- 566 Giladi, A., Cohen, M., Medaglia, C., Baran, Y., Li, B., Zada, M., et al. (2020). Dissecting cellular
567 crosstalk by sequencing physically interacting cells. *Nat. Biotechnol.* 38, 629–637.
- 568 Haass, N. K., and Herlyn, M. (2005). Normal human melanocyte homeostasis as a paradigm for
569 understanding melanoma. *J. Investig. Dermatol. Symp. Proc.* 10, 153–163.
- 570 Haemmerle, M., Stone, R. L., Menter, D. G., Afshar-Kharghan, V., and Sood, A. K. (2018). The Platelet
571 Lifeline to Cancer: Challenges and Opportunities. *Cancer Cell* 33, 965–983.
- 572 Heldin, C.-H., Lu, B., Evans, R., and Gutkind, J. S. (2016). Signals and Receptors. *Cold Spring Harb.*
573 *Perspect. Biol.* 8, a005900.
- 574 Hubert M., Pison G., Struyf A., Van Aelst S., editors. Theory and applications of recent robust methods.
575 Birkhäuser; 2012 Dec 6.
- 576 Jin, S., Guerrero-Juarez, C. F., Zhang, L., Chang, I., Myung, P., Plikus, M. V., et al. (2020). Inference and
577 analysis of cell-cell communication using CellChat. *Cold Spring Harbor Laboratory*,

- 578 2020.07.21.214387. doi:10.1101/2020.07.21.214387.
- 579 Kirilovsky, A., Marliot, F., El Sissy, C., Haicheur, N., Galon, J., and Pagès, F. (2016). Rational bases for
580 the use of the Immunoscore in routine clinical settings as a prognostic and predictive biomarker in
581 cancer patients. *Int. Immunol.* 28, 373–382.
- 582 Kumar, M. P., Du, J., Lagoudas, G., Jiao, Y., Sawyer, A., Drummond, D. C., et al. (2018). Analysis of
583 Single-Cell RNA-Seq Identifies Cell-Cell Communication Associated with Tumor Characteristics.
584 *Cell Rep.* 25, 1458–1468.e4.
- 585 Lippitz, B. E., and Harris, R. A. (2016). Cytokine patterns in cancer patients: A review of the correlation
586 between interleukin 6 and prognosis. *Oncoimmunology* 5, e1093722.
- 587 Liu, J., Lichtenberg, T., Hoadley, K. A., Poisson, L. M., Lazar, A. J., Cherniack, A. D., et al. (2018). An
588 Integrated TCGA Pan-Cancer Clinical Data Resource to Drive High-Quality Survival Outcome
589 Analytics. *Cell* 173, 400–416.e11.
- 590 Mathew, E., Brannon, A. L., Del Vecchio, A., Garcia, P. E., Penny, M. K., Kane, K. T., et al. (2016).
591 Mesenchymal Stem Cells Promote Pancreatic Tumor Growth by Inducing Alternative Polarization
592 of Macrophages. *Neoplasia* 18, 142–151.
- 593 Messmer, M. N., Netherby, C. S., Banik, D., and Abrams, S. I. (2015). Tumor-induced myeloid
594 dysfunction and its implications for cancer immunotherapy. *Cancer Immunol. Immunother.* 64, 1–
595 13.
- 596 Morel, P. A., Lee, R. E. C., and Faeder, J. R. (2017). Demystifying the cytokine network: Mathematical
597 models point the way. *Cytokine* 98, 115–123.
- 598 Nath, A., and Leier, A. (2020). Improved cytokine-receptor interaction prediction by exploiting the
599 negative sample space. *BMC Bioinformatics* 21, 493.
- 600 Pagès, F., Mlecnik, B., Marliot, F., Bindea, G., Ou, F.-S., Bifulco, C., et al. (2018). International
601 validation of the consensus Immunoscore for the classification of colon cancer: a prognostic and
602 accuracy study. *Lancet* 391, 2128–2139.
- 603 Pomaznoy, M., Ha, B., and Peters, B. (2018). GOnet: a tool for interactive Gene Ontology analysis. *BMC*
604 *Bioinformatics* 19, 470.
- 605 Ramilowski, J. A., Goldberg, T., Harshbarger, J., Kloppmann, E., Lizio, M., Satagopam, V. P., et al.
606 (2015). A draft network of ligand–receptor-mediated multicellular signalling in human. *Nat.*
607 *Commun.* 6, 7866.
- 608 Reddy, J. K., Rao, M. S., Yeldandi, A. V., Tan, X. D., and Dwivedi, R. S. (1991). Pancreatic hepatocytes.
609 An in vivo model for cell lineage in pancreas of adult rat. *Dig. Dis. Sci.* 36, 502–509.
- 610 Robertson, A. G., Shih, J., Yau, C., Gibb, E. A., Oba, J., Mungall, K. L., et al. (2017). Integrative
611 Analysis Identifies Four Molecular and Clinical Subsets in Uveal Melanoma. *Cancer Cell* 32, 204–
612 220.e15.
- 613 Shao, X., Liao, J., Li, C., Lu, X., Cheng, J., and Fan, X. (2020). CellTalkDB: a manually curated database
614 of ligand-receptor interactions in humans and mice. *Brief. Bioinform.* doi:10.1093/bib/bbaa269.

- 615 Song, D., Yang, D., Powell, C. A., and Wang, X. (2019). Cell-cell communication: old mystery and new
616 opportunity. *Cell Biol. Toxicol.* 35, 89–93.
- 617 Theory and Applications of Recent Robust Methods | Mia Hubert | Springer Available at:
618 <https://www.springer.com/gp/book/9783764370602> [Accessed June 19, 2020].
- 619 Thorsson, V., Gibbs, D. L., Brown, S. D., Wolf, D., Bortone, D. S., Ou Yang, T.-H., et al. (2018). The
620 Immune Landscape of Cancer. *Immunity* 48, 812–830.e14.
- 621 Trosko, J. E., and Ruch, R. J. (1998). Cell-cell communication in carcinogenesis. *Front. Biosci.* 3, d208–
622 36.
- 623 Voutsadakis, I. A. (2014). Thrombocytosis as a prognostic marker in gastrointestinal cancers. *World J.*
624 *Gastrointest. Oncol.* 6, 34–40.
- 625 Wei, C.-J., Xu, X., and Lo, C. W. (2004). Connexins and cell signaling in development and disease.
626 *Annu. Rev. Cell Dev. Biol.* 20, 811–838.
- 627 West, J., and Newton, P. K. (2019). Cellular interactions constrain tumor growth. *Proc. Natl. Acad. Sci.*
628 *U. S. A.* 116, 1918–1923.
- 629 Weston, B. R., Li, L., and Tyson, J. J. (2018). Mathematical Analysis of Cytokine-Induced Differentiation
630 of Granulocyte-Monocyte Progenitor Cells. *Front. Immunol.* 9, 2048.
- 631 Wilson, M. R., Close, T. W., and Trosko, J. E. (2000). Cell Population Dynamics (Apoptosis, Mitosis,
632 and Cell–Cell Communication) during Disruption of Homeostasis. *Exp. Cell Res.* 254, 257–268.
- 633 Wolf, B. J., Choi, J. E., and Exley, M. A. (2018). Novel Approaches to Exploiting Invariant NKT Cells in
634 Cancer Immunotherapy. *Front. Immunol.* 9, 384.
- 635 Yahaya, S. S. S., Othman, A. R., and Keselman, H. J. (2004). Testing the Equality of Location Parameters
636 for Skewed Distributions Using S1 with High Breakdown Robust Scale Estimators. in *Theory and*
637 *Applications of Recent Robust Methods* (Birkhäuser Basel), 319–328.
- 638 Yáñez, A., Coetzee, S. G., Olsson, A., Muench, D. E., Berman, B. P., Hazelett, D. J., et al. (2017).
639 Granulocyte-Monocyte Progenitors and Monocyte-Dendritic Cell Progenitors Independently
640 Produce Functionally Distinct Monocytes. *Immunity* 47, 890–902.e4.
- 641 Zhang, J., Hou, L., Zhao, D., Pan, M., Wang, Z., Hu, H., et al. (2017). Inhibitory effect and mechanism of
642 mesenchymal stem cells on melanoma cells. *Clin. Transl. Oncol.* 19, 1358–1374.
- 643 Zhou, J. X., Taramelli, R., Pedrini, E., Knijnenburg, T., and Huang, S. (2017). Extracting Intercellular
644 Signaling Network of Cancer Tissues using Ligand-Receptor Expression Patterns from Whole-
645 tumor and Single-cell Transcriptomes. *Sci. Rep.* 7, 8815.
- 646
- 647

648 Figure Legends

649

650 Figure 1. Overview of workflow showing the transition from data sources to results.

651

652 Figure 2. Illustration of the probabilistic model and edge weight computations. (A) For a given cell-cell
653 communication edge, (B) per patient values are used to 'look up' probabilities from the distributions
654 learned from all TCGA data. Those probabilities are then used to compute an edge weight.

655

656 Figure 3. Diagram of how differentially weighted edges were determined. Three samples of edge weights
657 were taken from the pool by tissue source. Then matching the sample proportions in the clinical features,
658 permutations were sampled and used for computing randomized S_I statistics. Each sample was used to
659 produce 1 million permuted statistics, and taken together, the millionth percentile was used as a cutoff in
660 determining important edges.

661

662 Figure 4. Top edges (by S_I scores) that can distinguish tissue types. Each point represents a tumor sample
663 and each panel represents one edge. (A) EdgeID 605551, Melanocytes-MIA-CDH19-Melanocyte SKCM
664 red, UVM blue, BRCA purple, PAAD orange. (B) EdgeID 687457, MSC-TFPI-F3-MS, PAAD red. (C)
665 EdgeID 968128, Sebocytes-WNT5A-FZD6- Sebocytes, LUSC red, LUAD blue, HNSC purple. (D)
666 EdgeID 1049823, Th2 cells-IL4-IL2RG-Megakaryocytes, STAD red, READ blue, COAD purple, ESCA
667 orange.

668

669 Figure 5. (A) Median values for each differentially weighted cell-cell edge (DWE) for the PFI categories
670 (in row, DWE edges in columns). (B) Examples of differentially weighted edges.

671

672 Figure 6. Edge member dominance in DWEs shown by log10 counts of cell types.

673

674 Figure 7. High probability edges (DWEs) from PFI contrasts form predictive connected subnetworks.
675 Color indicates the magnitude and direction of S_I statistics (+ / -).

676

677 Figure 8. Informative edges selected by XGBoost models for prediction within study. Color indicates
678 information gain.

679

680 Figure 9. Cell-cell interaction diagram demonstrating complexity in communication with three cell types
681 that produce the IL1B ligand that have two possible binding partners on the same receptor bearing cell.
682 Edge weight violin plots are shown for two STAD PFI groups, short (left) and long (right) PFI.

Figure 1

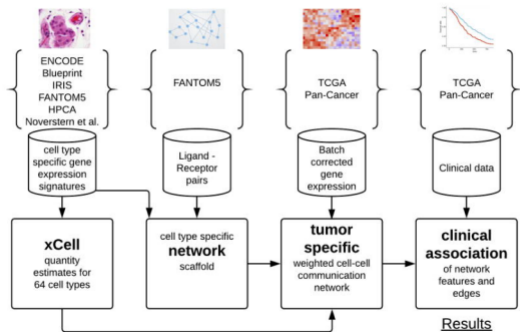
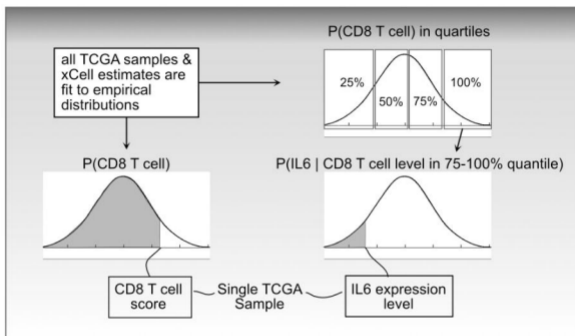


Figure 2

A. CD8 T cell \longrightarrow IL6 \longrightarrow IL6R \longrightarrow NK cell

B.



$$P(\text{CD8 T cell}) * P(\text{IL6} | \text{CD8 T cell in 75-100\% quantile}) = 0.86 * 0.21$$

$$P(\text{NK cell}) * P(\text{IL6R} | \text{NK cell in 25-50\% quantile}) = 0.77 * 0.42$$

$$\text{edge weight for this example} = 0.86 * 0.21 * 0.77 * 0.42 = 0.06$$

* distribution look-ups for the NK cell side not shown

Figure 3

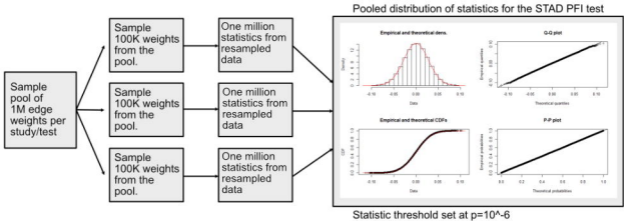
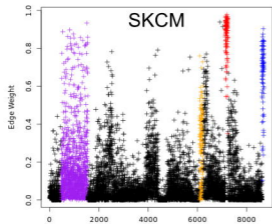
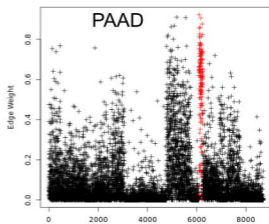


Figure 4

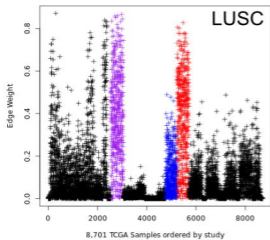
A



B



C



D

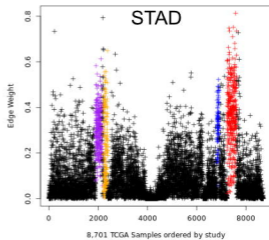
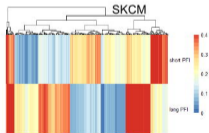
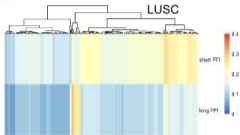


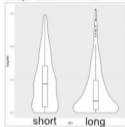
Figure 5

A

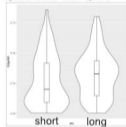


B

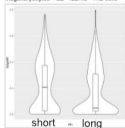
COAD, PFI test
Sebocyte - COL6A1 - ITGA1 - MSC



ESCA, PFI test
Epithelial - LAMC2 - ITGB4 - Epithelial



STAD, PFI test
Megakaryocytes - IL2 - IL2RG - Th2 cells



SKCM, Stage test
GMP - VIM - CD44 - naive B cells

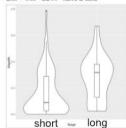


Figure 7

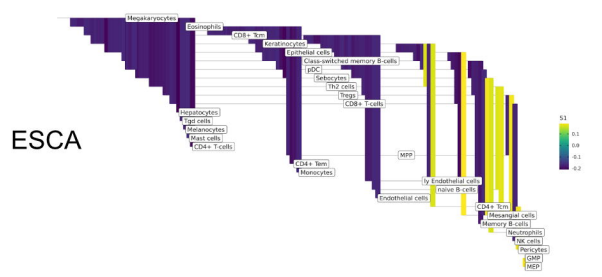
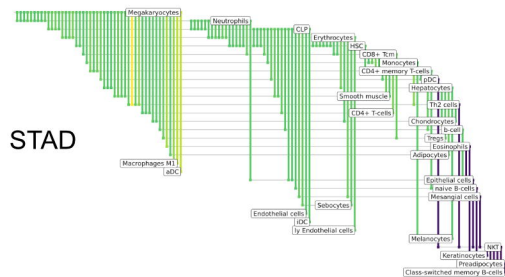
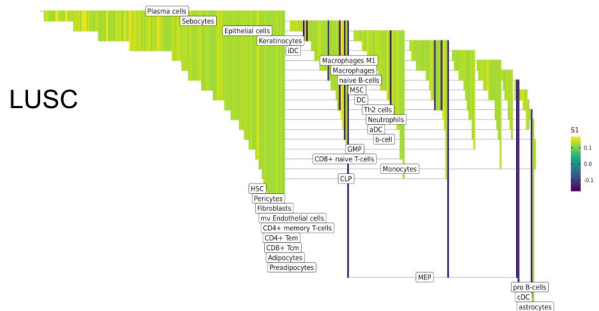
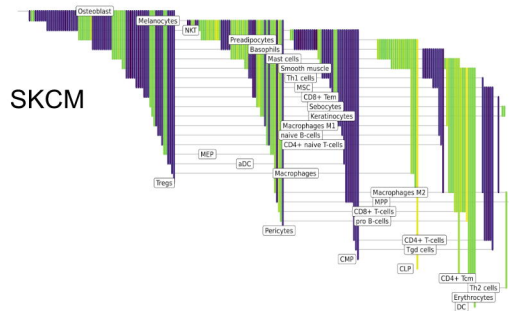


Figure 8

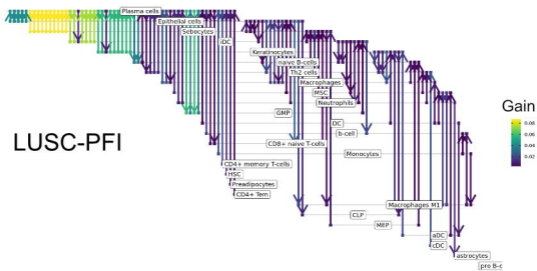
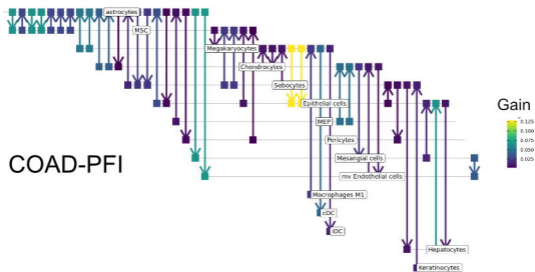
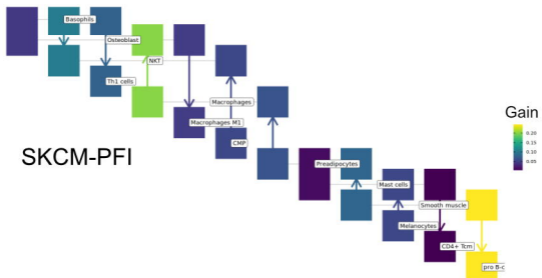


Figure 9

